Giant spin and orbital moment anisotropies of a Cu-phthalocyanine monolayer

S. Stepanow,[1] A. Mugarza,[1] G. Ceballos,[1] P. Moras,[2] J. C. Cezar,[3] C. Carbone,[2] and P. Gambardella[1,4]
[1]*Centre d'Investigaciò en Nanociència i Nanotecnologia (ICN-CSIC), UAB Campus, E-08193 Bellaterra, Spain*
[2]*Istituto di Struttura della Materia, Consiglio Nazionale delle Ricerche, Area Science Park, I-34012 Trieste, Italy*
[3]*European Synchrotron Radiation Facility, BP 220, F-38043 Grenoble, France*
[4]*Institució Catalana de Recerca i Estudis Avançats (ICREA), E-08100 Barcelona, Spain*
(Received 28 April 2010; revised manuscript received 4 June 2010; published 8 July 2010)

The magnetism of a Cu-phthalocyanine (CuPc) monolayer on Ag(100) was investigated using x-ray magnetic circular dichroism (XMCD) and ligand-field multiplet calculations. Contrary to other metal-Pc adsorbed on metals, we show that the local CuPc moment survives the interaction with the electronic states of the substrate and presents enhanced susceptibility with respect to bulk powder samples. Our measurements reveal extraordinary orbital moment anisotropy (500%) and an anisotropic spin dipole moment up to twice the isotropic spin in a metal-organic layer. A complete description of the orbital, spin, and spin-orbit operators is provided based on the XMCD sum rules.

DOI: 10.1103/PhysRevB.82.014405 PACS number(s): 75.70.Ak, 75.70.Tj, 78.70.Dm, 81.07.Pr

I. INTRODUCTION

Extensive research has been undertaken in the last five years to study hybrid systems combining metal and molecular layers for the design of novel magnetic devices.[1,2] Compounds that incorporate one or more local spins into an organic framework integrate a wide spectrum of magnetic properties with additional and sometime exotic electronic functionalities, such as Kondo and Coulomb blockade effects,[3] giant negative magnetization,[4] magnetochiral dichroism,[5] and site-specific control of magnetic anisotropy.[6] The understanding of these complexes would be greatly improved by insight into their microscopic magnetic behavior, in particular, by the accurate determination of their spin and orbital moments as well as their anisotropies. This is of crucial importance when metal-organic molecules are interfaced with a magnetic or nonmagnetic metal as part of a hybrid layer since both their electronic and magnetic susceptibilities may differ significantly from those of the bulk compounds.

Molecules belonging to the metal-phthalocyanine (MePc) and porphyrin family represent archetypal metal-organic semiconductors that display excellent chemical stability and film growth properties. Their planar macrocyclic structure can accommodate a large variety of metal ions at their center [Fig. 1(a)], giving rise to many interesting magnetic phenomena, ranging from paramagnetism (Mn, Fe, Co, CuPc) to one-dimensional Heisenberg (CuPc) (Ref. 7), and single-molecule magnet behavior ($TbPc_2$),[8] as well as exchange coupling to metal[9–13] and molecular layers.[14] Recent scanning-tunneling microscopy (STM) studies, however, have shown that the magnetic moment of MePc deposited on nonmagnetic metallic substrates is very often screened through the Kondo interaction[14–16] or even completely quenched by hybridization.[17] Thus, in the interface regime, the physical properties of MePc appear to be dominated by the interaction with metal states, significantly reducing their magnetic response and usefulness for applications.

Here, we focus on CuPc, *magnetic blue*,[18] a model spin 1/2 system that has recently attracted attention due to the possibility to control intermolecular magnetic coupling in thick films[19] and its relatively large spin-diffusion length.[20] We exploit the surface sensitivity of x-ray magnetic circular dichroism (XMCD) measurements to submonolayer amounts of magnetic atoms[21,22] to gain element-specific quantitative information on the magnetic moment of the Cu ions in a hybrid CuPc/metal system. By combining STM, XMCD, x-ray natural linear dichroism (XNLD), and atomic multiplet calculations, we show that a CuPc monolayer in contact with Ag(100) displays the spin magnetic moment expected of the Cu^{2+} ion in a tetragonally distorted ligand field, with a susceptibility enhancement of about a factor 9 over bulk CuPc powders. Angle-dependent XMCD measurements reveal extraordinarily strong Cu spin dipole moment and orbital-moment anisotropies. The spin dipole moment is up to two times larger compared to the isotropic spin moment whereas the orbital moment changes by 500% from the in-plane to the out-of-plane directions. These measurements, interpreted with the aid of ligand-field multiplet calculations, also provide a long-sought experimental verification of the role played by the spin dipole moment in the quantitative interpretation of XMCD of $3d$ metals.[23–28]

II. EXPERIMENT

The experiments were performed at beamline ID08 of the European Synchrotron Radiation Facility (ESRF). The deposition and adsorption configurations of CuPc on Ag(100) were studied in detail by means of STM and low-energy electron diffraction (LEED) in a dedicated setup prior to the beamtime.[29] The sample preparation procedure was reproduced at the ESRF, where CuPc films were evaporated onto a sputter-annealed Ag(100) single crystal held at room temperature from a molecular-beam source heated to 600 K, after degassing the 99% pure powder material (Sigma Aldrich) to 500 K for 24 h in ultrahigh vacuum. The base pressure was 1×10^{-10} mbar. *In situ* STM and LEED were used to monitor the growth of 1 monolayer (ML) CuPc. STM measurements were performed in a crosslike geometry over a distance of ±2 mm from the sample center and LEED was performed over the whole sample surface to check the layer

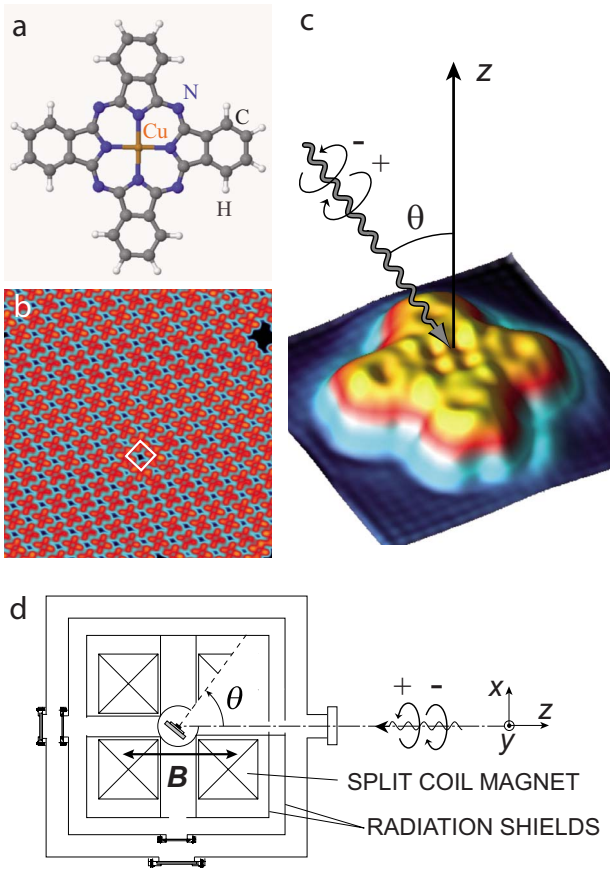

FIG. 1. (Color online) (a) Ball and stick model of CuPc. (b) STM image of 1 ML CuPc on Ag(100), image size 170×170 Å^2, bias voltage 1.4 V, tunnelling current 100 pA. The square indicates the CuPc unit cell. (c) Experimental geometry. STM image acquired at bias voltage −5 mV, tunnelling current 54 pA. (d) Diagram of the XMCD setup.

homogeneity and make sure that no second-layer molecules were present. The sample was subsequently transferred into the XMCD end station without breaking ultrahigh vacuum and cooled to $T=6$ K. For comparison, a powder CuPc sample was also measured in the same experimental conditions. STM shows that CuPc adsorb planarly on Ag(100) forming a superlattice with a 14.5 Å square unit cell, as shown in Fig. 1(b). Figures 1(c) and 1(d) show the geometry employed in the x-ray absorption measurements. X-ray absorption spectra (XAS) were measured at the $L_{2,3}$ edges of Cu in the total electron yield mode and normalized by the incident photon flux given by the photocurrent of an Au mesh placed between the last optical element of the beamline and the sample. The footprint of the beam at normal incidence was about 1×0.1 mm^2 at full width half maximum (FWHM). We used both circularly and linearly polarized light with 99% polarization in magnetic fields of up to $\mathbf{B}=\pm5$ T applied parallel to the incident-beam direction, as shown in Fig. 1(d). Spectra recorded with circularly polarized light with photon helicity parallel and antiparallel to **B** are indicated as I^+ and I^-, respectively. The XMCD signal is defined as $I^- - I^+$. In order to probe the anisotropy of the CuPc ML, the sample was rotated about the $\hat{\mathbf{y}}$ axis by an angle θ comprised between 0° (normal incidence) and 75° (grazing incidence). Linearly polarized spectra recorded with **E** in plane and nearly out of plane were recorded by switching the polarization from $\hat{\mathbf{y}}$ to $\hat{\mathbf{x}}$ at $\theta=70°$ and indicated in the following as $I^{\parallel}_{70°}$ and $I^{\perp}_{70°}$, respectively. The equivalent density of the Cu ions contained in 1 ML CuPc is 4% of the Ag atoms in a (100) layer; this made it necessary to average multiple spectra obtained by switching both light polarization and applied magnetic field in order to obtain a satisfactory signal-to-noise ratio at the Cu edge. Moreover, due to the intensity tail of the Ag M absorption edges, the Cu XAS are superimposed onto a strong substrate background intensity [inset, Fig. 2(b)], which needs to be subtracted to properly normalize the XMCD signal for quantitative sum-rule analysis, as reported in Refs. 6 and 30. No evidence of sample degradation was detected due to beam damage or residual gas contamination during the experiments.

III. MULTIPLET CALCULATIONS

A. Hamiltonian

In order to interpret the magnetic properties and XAS measurements of the CuPc ML, we used ligand-field multiplet theory.[31–33] We wrote a code to calculate the XAS of metal ions for arbitrary photon polarization and incidence angle with respect to the symmetry axes of the molecules and applied magnetic-field direction. The Hamiltonian of initial and final states, e.g., $2p^63d^N$ and $2p^53d^{N+1}$ for the L edge of transition metals, respectively, is separately diagonalized and the XAS calculated from the sum of all dipole-allowed transitions for an electron excited from the occupied $2p$ level into an unoccupied $3d$ level. In the crystal-field limit, the ground state is given by a single electronic configuration d^N (where N is the number of valence d electrons), split in energy by electron repulsion and ligand-field potential. The single-ion Hamiltonian contains the usual atomic terms for the electron kinetic energy, nuclear attraction, electron repulsion, and spin-orbit coupling. The first two terms yield the average energy of the configuration. The electron-electron repulsion is treated in the Hartree-Fock approximation and expressed by the Slater-Condon-Shortley parameters (F_i and G_i). The spherical part of the electron-electron interaction is added to the average energy of the configuration. The parameters F_i and G_i and the spin-orbit coupling constants are obtained using the atomic theory code developed by Cowan.[31] The molecular environment is modeled by an electric potential either by the usual parameters that reflect the point-group symmetry of the metal-ion site or by direct evaluation of the potential with point charges at the ligand locations. The crystal field is only applied to the outer shell since the core hole in the excited state is well screened by the other electrons. The many-electron wave function of a single configuration is represented by a linear combination of determinantal product states with basis wave functions of the form $R_n(r)Y^k_m(\theta,\phi)\chi(\sigma)$, which separates into the radial part $R_n(r)$, the spherical harmonics Y^k_m for the angular dependence, and the spin function $\chi(\sigma)$. The matrix elements of the radial part for the different terms of the Hamiltonian are given by the Slater-Condon-Shortley parameters and crystal-field potential parameters. The nonspherical part of the total

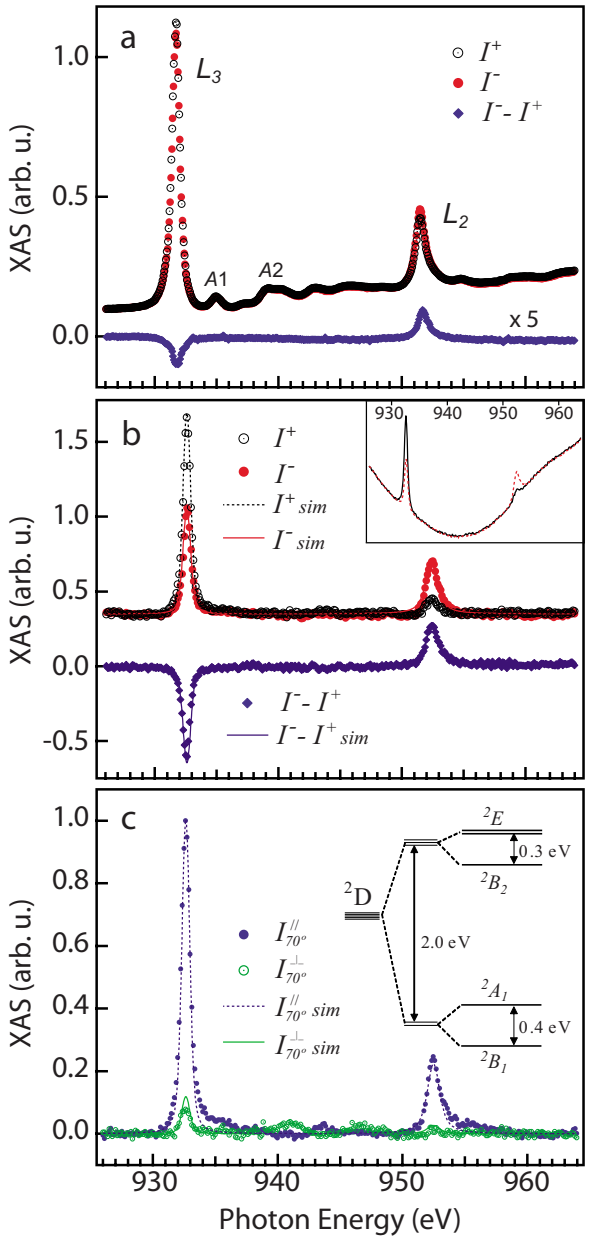

FIG. 2. (Color online) Circularly polarized $L_{2,3}$ XAS and XMCD of (a) bulk CuPc powder and (b) 1 ML CuPc/Ag(100) at normal incidence. $\mathbf{B}=5$ T and $T=6$ K. (c) Linearly polarized XAS of 1 ML CuPc/Ag(100) recorded with $\mathbf{E}$ in-plane ($I^{\parallel}_{70°}$) and 70° out-of-plane ($I^{\perp}_{70°}$). Inset: crystal-field diagram. The spectra in (b) and (c) are shown after Ag background subtraction. The inset in (b) reports the raw $I^{\pm}$ data. Solid and dashed lines are simulated spectra (see text).

Hamiltonian is numerically diagonalized, including the Zeeman energy term,

$$H_Z = \sum_{i=1}^{N} \frac{\mu_B}{\hbar} \mathbf{B} \cdot (2\mathbf{s}^i + \mathbf{l}^i), \tag{1}$$

in initial and final-state Hamiltonians. Here, $\mathbf{s}^i$ and $\mathbf{l}^i$ are the one-electron spin and orbital kinetic momentum operators that add up to give the total atomic spin ($\mathbf{S}$) and orbital moments ($\mathbf{L}$). The XAS spectra are calculated with the transition matrix elements for the electric-dipole operator for arbitrary photon polarization and incidence angles. At finite temperatures the initial states are weighted according to the Boltzmann distribution for the calculation of the transition probabilities.

B. Spin dipole operator

In low-symmetry environments, the anisotropic charge distribution that results from strongly directional bonds or crystal field induces an inhomogeneous spatial distribution of the spin density over the atomic unit cell.[24] Such a spin anisotropy can be expressed as a nonzero spin dipole moment, which affects the XMCD intensity through the angular dependence of the transition-matrix elements. The spin dipole momentum operator of a single electron is defined as

$$\boldsymbol{t} = \boldsymbol{s} - \frac{3\boldsymbol{r}(\boldsymbol{r}\cdot\boldsymbol{s})}{r^2}. \tag{2}$$

The components of $\boldsymbol{t}$ are, accordingly,

$$t_x = \left(1 - 3\frac{x^2}{r^2}\right)s_x - 3\frac{xy}{r^2}s_y - 3\frac{xz}{r^2}s_z, \tag{3}$$

$$t_y = \left(1 - 3\frac{y^2}{r^2}\right)s_y - 3\frac{yx}{r^2}s_x - 3\frac{yz}{r^2}s_z, \tag{4}$$

$$t_z = \left(1 - 3\frac{z^2}{r^2}\right)s_z - 3\frac{zx}{r^2}s_x - 3\frac{zy}{r^2}s_y. \tag{5}$$

Using the spin raising and lowering operators, s_+ and s_-, and expressing the polynomials of the spatial coordinates by spherical harmonics, we obtain

$$t_x = \sqrt{\frac{\pi}{5}}[(Y_2^0 - \sqrt{6}Y_2^{-2})\hat{s}_+ + (Y_2^0 - \sqrt{6}Y_2^2)\hat{s}_- + \sqrt{6}(Y_2^1 - Y_2^{-1})\hat{s}_z], \tag{6}$$

$$t_y = -i\sqrt{\frac{\pi}{5}}[(Y_2^0 + \sqrt{6}Y_2^{-2})\hat{s}_+ + (Y_2^0 - \sqrt{6}Y_2^2)\hat{s}_- + \sqrt{6}(Y_2^1 + Y_2^{-1})\hat{s}_z], \tag{7}$$

$$t_z = \sqrt{\frac{4\pi}{5}}\left[-2Y_2^0\hat{s}_z - \frac{\sqrt{6}}{2}(Y_2^{-1}\hat{s}_+ - Y_2^1\hat{s}_-)\right], \tag{8}$$

in which form their matrix elements can be easily evaluated. For an N-electron atom, the intra-atomic spin dipole operator is defined as $\mathbf{T}=\Sigma_{i=1}^{N}\mathbf{t}^i$, whose spatial components $\alpha=x,y,z$ can be written as

$$T_\alpha = \sum_i \sum_\beta \left(\delta_{\alpha\beta} - \frac{3}{(r^i)^2} r^i_\alpha r^i_\beta\right) s^i_\beta = \sum_i \sum_\beta Q^i_{\alpha\beta} s^i_\beta, \tag{9}$$

where $Q^i_{\alpha\beta}$ is the charge quadrupole tensor of the ith one-electron state. Note that only in the absence of spin-orbit coupling the expectation values of the charge and spin op-

erators in Eq. (9) can be decoupled and separately evaluated. Additionally, if the sample is magnetically saturated parallel to α, one has $s^i_\alpha = s^i$ and the expectation value of T_α reduces to

$$\langle T_\alpha \rangle = \sum_i \langle Q^i_{\alpha\alpha} \rangle s^i. \tag{10}$$

As each $Q^i_{\alpha\beta}$ is a traceless tensor, it follows that

$$\sum_\alpha \langle T_\alpha \rangle = \sum_i s^i \sum_\alpha \langle Q^i_{\alpha\alpha} \rangle = 0. \tag{11}$$

This is the "spin dipole sum rule," which allows to average out the **T** contribution to the effective spin moment measured by XMCD (Ref. 46) by performing either three separate measurements along orthogonal directions or recording a single magic angle spectrum at $\theta = 54.7°$, for symmetries D_{2h}, C_4, or higher.[24]

C. Expectation values of *L*, *S*, and *T*

The expectation values of the atomic kinetic momentum operators $\mathbf{M}=\mathbf{L}$, **S**, and **T** of state $|\Psi\rangle$ projected onto the direction $\boldsymbol{e}_\theta$ were calculated as

$$\langle M_\theta \rangle = \langle \Psi | \mathbf{M} \cdot \boldsymbol{e}_\theta | \Psi \rangle = (\boldsymbol{e}_\theta \cdot \boldsymbol{e}_x)\langle M_x \rangle + (\boldsymbol{e}_\theta \cdot \boldsymbol{e}_y)\langle M_y \rangle + (\boldsymbol{e}_\theta \cdot \boldsymbol{e}_z)\langle M_z \rangle. \tag{12}$$

To take finite-temperature effects into account, the moments were weighted by the Boltzmann distribution according to

$$\langle M_\theta(T) \rangle = \frac{1}{Z} \sum_\Psi \langle M^\Psi_\theta \rangle e^{-E_\Psi / k_B T}, \tag{13}$$

where $Z = \Sigma_\Psi e^{-E_\Psi / k_B T}$.

D. CuPc parameters

The Cu ion was represented by a d^9 configuration corresponding to an oxidation state +2. The molecular environment was modeled by a C_{4v} crystal-field potential defined by the parameters $10D_q = 2.0$, $D_s = 0.1$, and $D_t = 0.0$ eV. These parameters were obtained as those giving the best simultaneous fit of the linear and circular XAS and XMCD features. The temperature was taken from the experiment to be $T = 6$ K. The spin-orbit coupling constants for $2p$ and $3d$ subshells are $\lambda_{2p} = 13.228$ and $\lambda_{3d} = 0.102$ eV, respectively. The spectra were broadened by Lorentzians with FWHM of 0.15 eV and 0.45 eV at the L_3 and L_2 edge, respectively, in order to account for the finite lifetime of the core hole. An additional convolution with a Gaussian function with FWHM of 0.25 eV was performed to take into account the experimental resolution. We note that the calculations reported in this paper treat only $2p^6 3d^9 \rightarrow 2p^5 3d^{10}$ transitions. This case is equivalent to a single-hole calculation, for which electron-correlation effects are absent. However, our code can treat any number of electrons and include configuration interactions if necessary. In the present case, the relative simplicity of the calculations favors a straightforward analysis of the interplay of spin-orbit, crystal-field effects, and magnetic moments.

IV. RESULTS AND DISCUSSION

A. Magnetic moment and electronic configuration of 1 ML CuPc

We present first the measurements obtained on polycrystalline CuPc powders, for which the average alignment of the molecules with respect to the x-ray wave vector is random.[34] Consistently with previous reports,[35–37] the XAS of CuPc, shown in Fig. 2(a), feature two main lines separated by about 20 eV, reflecting the transitions from the Cu $2p_{1/2,3/2}$ manifolds into an empty orbital with predominant $3d_{x^2-y^2}$ character. The higher energy satellites $A1$ and $A2$ and their L_2 replicas are assigned to less intense transitions into the e_g molecular orbital and $4s$ states, respectively.[37] The XMCD of the bulk CuPc powder, for which no comparison exists in the literature, is rather weak even in an applied magnetic field of 5 T. The XMCD/XAS asymmetry, measured at the L_2 edge to minimize saturation effects, is a mere 6%, much smaller than expected for an isolated paramagnetic spin at the same field and temperature. This behavior changes drastically upon adsorption of 1 ML CuPc on Ag(100). In contrast with the powder, the CuPc ML presents a large XMCD asymmetry (57%) at 5 T [Fig. 2(b)], indicative of a strong magnetic response. As the field dependence of the XMCD is nearly linear, the magnetic susceptibility of the ML turns out to be about nine times larger compared to the powder. This enhancement is attributed in part to angle averaging effects (a factor 1.8, calculated numerically by averaging over the solid angle) and in part to the absence of antiferromagnetic interactions favored by Cu-Cu stacking in CuPc crystals.[7]

The XMCD measurements show that the magnetic moment of CuPc is much more robust upon adsorption compared to that of other planar metal-organic macrocycles such as FePc and CoPc.[14–17] This may appear puzzling given that FePc and CoPc, which have bulk intermediate $S=1$ and $S=1/2$ configurations, respectively,[38–41] should display a stronger tendency to sustain a local moment compared to Cu due to the larger number of unoccupied states in the $3d$ shell. Moreover, it has been shown by photoemission that the interaction of CuPc with a metal substrate can lead to the complete reduction of the Cu oxidation state.[42] Our STM measurements and density-functional calculations[29] also indicate that the interaction between CuPc and Ag(100) is very strong. The molecules rotate in the plane by 30° with respect to the high-symmetry [011] Ag direction to maximize charge transfer (about one electron) from the substrate to C and N atoms, and rest at a distance of 2.4 Å from the surface, i.e., closer than what reported for nonmagnetic CoPc on Au(111).[17] Notwithstanding such a strong interaction, the XAS spectra clearly show the unoccupied character of the $3d$ states in 1 ML CuPc. The symmetry of the $3d$ hole is particularly evident by measuring the linearly polarized XAS at grazing incidence [Fig. 2(c)]. Very strong XNLD effects are observed as the intensity of the main L_3 and L_2 lines is maximal for parallel alignment of **E** with the surface plane and minimal for **E** oriented out of plane. Note that the XNLD extrapolates to 100% for **E** perpendicular to the surface and does not show a noticeable dependence on field or temperature from 300 to 6 K.

Ligand field multiplet calculations were used to simulate the XAS and derive the electronic configuration of 1 ML CuPc, as described in Sec. III D. The results of the XAS calculations are reported in Figs. 2(b) and 2(c) as solid lines. The agreement between experiment and model is excellent, allowing us to simulate simultaneously the XAS, XMCD, and XNLD in a quantitative way. The diagram in Fig. 2(c) shows the energy-level scheme of the Cu $3d$ states corresponding to the optimal crystal-field parameters reported in Sec. III A. The Cu ground state in 1 ML CuPc/Ag(100) is thus almost pure $^2B_1$, similar to that inferred from electron-paramagnetic-resonance (EPR) measurements for bulk CuPc,[7,43] which shows that the cupric ion is only weakly perturbed by the interaction with the substrate despite the strong Ag-CuPc charge transfer. This finding is corroborated by the fact that the powder spectra can be simulated to a very good degree of accuracy using the same crystal-field parameters as the ML, apart from the magnitude of the XMCD intensity. According to density-functional calculations of the CuPc monomer, the empty b_{1g} orbital is an antibonding Cu-N state with 27% N $2p$ character and fully spin-polarized 57% Cu $3d_{x^2-y^2}$ contribution.[44] The $3d_{x^2-y^2}$ state is therefore expected to dominate the magnetic properties of the CuPc ML with unusual consequences due to the combined effects of spin-orbit coupling and the planar symmetry enforced by the substrate.

B. Angle-dependent XAS intensity and XMCD sum rules

The Cu magnetic moment can be estimated quantitatively by means of the XMCD sum rules, which relate the L_3 and L_2 XMCD intensities to the expectation values of the **L**, **S**, and **T** operators projected on to the x-ray incidence direction θ, according to[45,46]

$$\langle L_\theta \rangle = -\frac{2q_\theta}{I^{ISO}} n_h, \tag{14}$$

$$\langle S_\theta^{eff} \rangle = 2\langle S_\theta \rangle + 7\langle T_\theta \rangle = -\frac{(9p_\theta - 6q_\theta)}{I^{ISO}} n_h, \tag{15}$$

where n_h represents the number of holes in the d shell, and

$$q_\theta = \int_{L_3+L_2} (I_\theta^- - I_\theta^+) d\varepsilon, \tag{16}$$

$$p_\theta = \int_{L_3} (I_\theta^- - I_\theta^+) d\varepsilon, \tag{17}$$

$$I^{ISO} = \int_{L_3+L_2} (I_\theta^+ + I_\theta^- + I_\theta^0) d\varepsilon. \tag{18}$$

Here, ε is the incident photon energy. I^0 corresponds to the absorption intensity measured with linear polarization parallel to the magnetization direction, i.e., to a measurement that requires a geometry orthogonal to that of the circular components I^+ and I^-, difficult to attain in practice. For this reason, it is usually approximated as $I_\theta^0 = (I_\theta^+ + I_\theta^-)/2$.[47] This approximation, although valid for metals, can lead to very large errors in the sum-rule analysis of ordered metal-organic compounds. The angular dependence of XAS has been studied by various authors in the case of molecules on surfaces[48] and anisotropic compounds in general.[27,49,50] Qualitatively, dipole-allowed transition matrix elements are largest when **E** is aligned parallel to an empty orbital. For orbitals having a C_4 symmetry rotation axis perpendicular to the substrate, $I_\theta^+ + I_\theta^-$ is expected to follow a function $f(\theta) = (1+\cos^2\theta)/2$, as given by the mixing of two orthogonal linearly polarized components, one in plane and the other tilted by θ with respect to the molecular plane. Indeed, a strong dependence on θ was found for the XAS of 1 ML CuPc, shown in Fig. 3(a). Note that, in order to compare spectra recorded at different angles and compensate for changes in the total electron yield, the raw data were first normalized to a common intensity value at 930 eV and background subtracted. The sum of L_3 and L_2 peak intensities so obtained is reported in Fig. 3(b), normalized to 1 at $\theta = 0°$. The agreement with the expected $f(\theta)$ dependence (dashed line) is very good. The energy-integrated intensities $\int_{L_3+L_2}(I_\theta^+ + I_\theta^-)d\varepsilon$ are found to scale as the peak values with a few percent uncertainty that depends on the choice of integration range and Ag background subtraction (error bars in Fig. 3). The largest error occurs at $\theta = 75°$ as the footprint of the x-ray beam becomes comparable to the lateral extension of the sample surface at grazing incidence. Symmetry considerations as well as the results of our XAS simulations show that $I_{0°}^0 = 0$ for 1 ML CuPc. Therefore, the isotropic intensity can be obtained simply as $I^{ISO} = I_{0°}^+ + I_{0°}^- = (I_\theta^+ + I_\theta^-)/f(\theta)$, as shown by the filled symbols in Fig. 3(b). This allows us to safely determine the expectation values of **L**, **S**, and **T** by means of Eqs. (14)–(18).

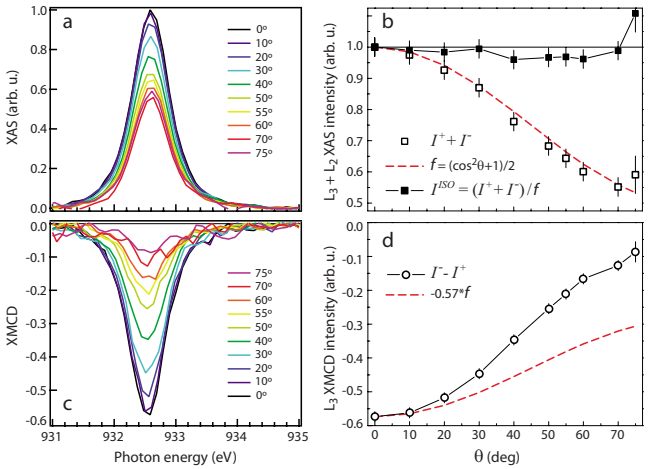

FIG. 3. (Color online) (a) Angular dependence of the L_3 XAS spectra at **B**=5 T and T=6 K. (b) Sum of L_3 and L_2 peak XAS values as a function of θ. (c) Angular dependence of the L_3 XMCD spectra. (d) L_3 XMCD peak values as a function of θ. The intensity scale is the same as (a) and (c). The dashed lines in (c) and (d) represent the function $f = (\cos^2\theta + 1)/2$ normalized to the first data point of the series. The full symbols in (b) show the isotropic XAS intensity obtained as $I^{ISO} = [I_+(\theta) + I_-(\theta)]/f(\theta)$ (see text).

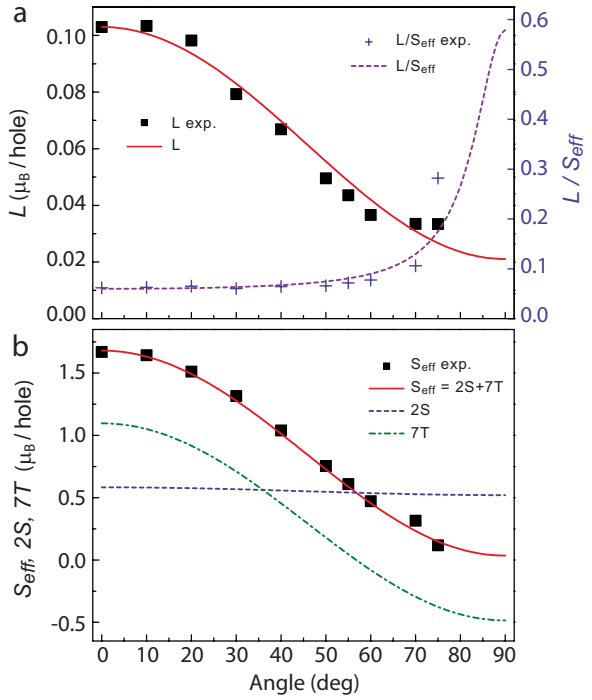

FIG. 4. (Color online) (a) Angular dependence of experimental (symbols) and calculated (solid line) expectation values of the orbital magnetic moment (L). The calculated values are shown after scaling by a factor $k=0.9$, see text. Crosses and dashed line refer to the right scale, reporting experimental and theoretical L/S_{eff} ratio, respectively. (b) Angular dependence of the effective spin moment ($S_{eff}=2S+7T$, symbols) and calculated S_{eff}, $2S$, and $7T$ values at 6 K, $B=5$ T.

C. Orbital and spin moment anisotropy of 1 ML CuPc

The angle-dependent XMCD intensity is found to reduce much faster compared to the decrease of $I_\theta^+ + I_\theta^-$ with θ [Fig. 3(d)]. This behavior could be, in principle, attributed to a strongly decreasing magnetization away from the easy axis in the presence of magnetic anisotropy.[30] However, no single-ion magnetic anisotropy is expected for a pure $S=1/2$ system. The explanation for this effect lies in the extraordinary anisotropy of both $\langle S_\theta^{eff}\rangle$ and $\langle L_\theta\rangle$, which determine the relative amplitude of the XMCD intensity through Eqs. (14)–(18). At normal incidence, taking $n_h=1$, we obtain $\langle L_{0^\circ}\rangle=0.10\pm0.02$ and $\langle S_{0^\circ}^{eff}\rangle=1.67\mu_B\pm0.08\mu_B$. The error bars have been calculated by varying the L_3 and L_2 integration limits over a few eV, in order to estimate the influence of involuntary offsets and noise in the XAS and XMCD baselines. These are particularly critical for the determination of $\langle L_\theta\rangle$, inducing a larger relative error compared to $\langle S_\theta^{eff}\rangle$ because of partial compensation of L_3 and L_2 intensities in Eq. (14). The absolute errors reported above are representative of the whole angle range, thus increasing their relative significance toward the in-plane direction.

The reported value of $\langle S^{eff}\rangle$ is clearly at variance with the spin magnetic moment ($2S=1$) expected for the $^2B_1$ state of CuPc. Moreover, $\langle S^{eff}\rangle$ reaches nearly zero and $\langle L\rangle$ decreases by a factor of 5 in the in-plane direction (Fig. 4). These apparent anomalies can be reconciled with the electronic structure of CuPc by analyzing the perturbative effects of the crystal field and spin-orbit interactions. For a pure $^2B_1$ orbital singlet, the orbital moment is entirely quenched, giving $\langle L_\theta\rangle=0\ \forall\ \theta$. $\mathbf{L}\cdot\mathbf{S}$ coupling treated to second order, however, mixes different nonzero orbital contributions into $\langle L_{0^\circ}\rangle$ and $\langle L_{90^\circ}\rangle$, given by $8k\lambda_{3d}/\Delta E_{B_2}$ and $2k\lambda_{3d}/\Delta E_E$, respectively, where $\Delta E_{B_2}(\Delta E_E)$ represents the energy of the B_2 (E) levels relative to the ground state and k is a so-called *covalence reduction* factor that takes into account electron delocalization effects that are not accounted for by the crystal-field model.[51] Our multiplet calculations reproduce this effect to a very good extent, matching the experimental $\langle L_\theta\rangle$ values after reduction by an (arbitrary) scaling factor $k=0.9$ [Fig. 4(a)]. We note that one may derive effective g-factor values for 1 ML CuPc from the XMCD data, giving $g_{0^\circ}=2.20$ and $g_{90^\circ}=2.04$, which compares to 2.17 and 2.05 obtained from EPR measurements of bulk CuPc.[7,43]

The strong anisotropy of $\langle S_\theta^{eff}\rangle$ necessarily calls attention to the $7\langle T_\theta\rangle$ term in Eq. (15), i.e., to the intra-atomic dipole spin moment that originates from the spatial distribution of the spin density. This moment is very often unknown and much debated in the literature.[23–28] Here, the combination of angle-dependent data and multiplet calculations allows us to determine and disentangle $7\langle T_\theta\rangle$ from $2\langle S_\theta\rangle$. The simulated and experimental $\langle S_\theta^{eff}\rangle$ agree to a very good level of accuracy without introducing scaling factors [Fig. 4(b)]. As expected, $\langle S_\theta\rangle$ turns out to be nearly isotropic, with a very weak angle dependence given by $\mathbf{L}\cdot\mathbf{S}$ coupling. $7\langle T_\theta\rangle$, on the other hand, exceeds by far the spin contribution, going from about $1.1\mu_B$ to $-0.5\mu_B$. Such a strong magnitude and anisotropy of $7\langle T_\theta\rangle$ have been predicted for low-symmetry systems,[24,27,28] but not measured experimentally so far. Our model can also be used to estimate the saturation values of the magnetic moments at 0 K, giving $2S=1(1)$, $L=0.20(0.045)$, and $7T=1.88(-0.95)\mu_B$ at $\theta=0^\circ(90^\circ)$.

The 1 ML CuPc/Ag(100) systems provides an ideal case to investigate the interplay of spin-orbit and crystal-field effects. The relative influence of these two interactions can be estimated by switching off the $3d$ spin-orbit coupling in the multiplet calculations. This yields a decrease of $\langle T_{0^\circ}\rangle(\langle T_{90^\circ}\rangle)$ of 8% (4%), in agreement with the assumption that the charge distribution is weakly affected by the spin orientation for relatively small spin-orbit coupling, a critical approximation of the spin dipole sum rule discussed in Sec. III B and Ref. 24. Given the value of the crystal-field splitting, the relative contribution of the spin dipole term in the XMCD sum rules is largely independent of temperature, contrary to what has been predicted for cubic systems.[26] Our calculations also show that a *magic angle* measurement yields $\langle T_{54.7^\circ}\rangle=0$ only if the spin-orbit coupling is set to zero. This is so even if the sample is not magnetically saturated, which is a consequence of the single-hole character of the CuPc ground state. However, when the spin-orbit coupling is turned on, the angle at which $\langle T_\theta\rangle=0$ changes to 56.8° [Fig. 4(b)].

D. Branching ratio

It is well known that the intensity ratio of the L_3 and L_2 absorption lines is not simply given by the degeneracy of

$2p_{3/2}$ and $2p_{1/2}$ core states. Spin-orbit splitting of the ground state and electrostatic core-valence interactions can induce sizeable deviations of the isotropic branching ratio, $\mathcal{B}=I^{ISO}(L_3)/[I^{ISO}(L_3)+I^{ISO}(L_2)]$, from the statistical 2/3 value.[52] Independently from the XMCD sum rules,[45,46] the analysis of the branching ratio can shed light on the spin state and spin-orbit splitting of transition-metal compounds.[52,53] In particular, if the electrostatic interactions between core hole and valence electrons are small or absent, as is the case for $2p^63d^9 \rightarrow 2p^53d^{10}$ transitions, it can be shown that[53,54]

$$\mathcal{B}=\frac{2}{3}-\frac{1}{3n_h}\mathcal{Z}, \tag{19}$$

where $\mathcal{Z}=\Sigma_{i=i}^{N}\mathbf{s}^i\cdot\mathbf{l}^i$ is the expectation value of the angular part of the spin-orbit operator in the valence state. From the experiment, we obtain $\mathcal{B}=0.73\pm0.03$ for 1 ML CuPc, which gives $\mathcal{Z}=-0.19\pm0.09$ through Eq. (19). Within the error, this value is found to be independent of θ, as expected for a scalar quantity. The calculated branching ratio is $\mathcal{B}=0.713$, giving $\mathcal{Z}=-0.14$, in fair agreement with the experiment.

V. CONCLUSIONS

In summary, we have shown that a CuPc monolayer displays enhanced susceptibility as well as robust spin and orbital local magnetic properties at the interface with a nonmagnetic noble metal, opposite to most other MePc species. This behavior is rationalized in terms of the planar symmetry of the Cu $^2B_1$ state, which couples weakly to the metal electrons despite the strong interaction and charge transfer between the molecular framework and the substrate. The intraatomic spin dipole moment is extraordinarily large, surpassing the magnetic spin moment by nearly a factor two in the perpendicular direction, and changing sign from out of plane to in plane. The orbital magnetic moment, although smaller compared to the spin, presents a giant anisotropic behavior due to the different admixture of excited states induced by the spin-orbit coupling when the spin points in plane or out of plane. Owing to its flat geometry, heavily distorted ligand field, and the presence of $3d$ spin-orbit coupling, this system represents an example of a strongly anisotropic $S=1/2$ hybrid metal-organic compound and a model for the interpretation of XMCD measurements of materials with localized electron properties.

ACKNOWLEDGMENTS

We thank P. Miedema and F. de Groot for critical discussions. Work was supported by the European Research Council (Starting Grant No. 203239 NOMAD), European Science Foundation (EUROCORES SANMAG), the Spanish Ministerio de Ciencia e Innovación (Grant No. MAT2007-62341), the Catalan Agència de Gestió d'Ajuts Universitaris i de Recerca (2009 SGR 695), and Italian MIUR (Grant No. PRIN 20087NX9YT). We acknowledge the ESRF for provision of beamtime.

[1] T. S. Santos, J. S. Lee, P. Migdal, I. C. Lekshmi, B. Satpati, and J. S. Moodera, Phys. Rev. Lett. **98**, 016601 (2007).
[2] L. Bogani and W. Wernsdorfer, Nature Mater. **7**, 179 (2008).
[3] J. Park, A. Pasupathy, J. I. Goldsmith, C. Chang, Y. Yaish, J. R. Petta, M. Rinkoski, J. P. Sethna, H. D. Abruna, P. L. McEuen, and D. C. Ralph, Nature (London) **417**, 722 (2002).
[4] R. S. Fishman and F. A. Reboredo, Phys. Rev. Lett. **99**, 217203 (2007).
[5] C. Train, R. Gheorghe, V. Krstic, L.-M. Chamoreau, N. S. Ovanesyan, G. L. J. A. Rikken, M. Gruselle, and M. Verdaguer, Nature Mater. **7**, 729 (2008).
[6] P. Gambardella, S. Stepanow, A. Dmitriev, J. Honolka, F. de Groot, M. Lingenfelder, S. S. Gupta, D. Sarma, P. Bencok, S. Stanescu, S. Clair, S. Pons, N. Lin, A. P. Seitsonen, H. Brune, J. Barth, and K. Kern, Nature Mater. **8**, 189 (2009).
[7] S. Lee, M. Yudkowsky, W. P. Halperin, M. Y. Ogawa, and B. M. Hoffman, Phys. Rev. B **35**, 5003 (1987).
[8] N. Ishikawa, M. Sugita, T. Ishikawa, S.-y. Koshihara, and Y. Kaizu, J. Am. Chem. Soc. **125**, 8694 (2003).
[9] T. Suzuki, M. Kurahashi, X. Ju, and Y. Yamauchi, J. Phys. Chem. B **106**, 11553 (2002).
[10] A. Scheybal, T. Ramsvik, R. Bertschinger, M. Putero, F. Nolting, and T. Jung, Chem. Phys. Lett. **411**, 214 (2005).
[11] H. Wende, M. Bernien, J. Luo, C. Sorg, N. Ponpandian, J. Kurde, J. Miguel, M. Piantek, X. Xu, P. Eckhold, W. Kuch, K. Baberschke, P. M. Panchmatia, B. Sanyal, P. M. Oppeneer, and O. Eriksson, Nature Mater. **6**, 516 (2007).
[12] M. Bernien, J. Miguel, C. Weis, M. E. Ali, J. Kurde, B. Krumme, P. M. Panchmatia, B. Sanyal, M. Piantek, P. Srivastava, K. Baberschke, P. M. Oppeneer, O. Eriksson, W. Kuch, and H. Wende, Phys. Rev. Lett. **102**, 047202 (2009).
[13] C. Iacovita, M. V. Rastei, B. W. Heinrich, T. Brumme, J. Kortus, L. Limot, and J. P. Bucher, Phys. Rev. Lett. **101**, 116602 (2008).
[14] X. Chen, Y.-S. Fu, S.-H. Ji, T. Zhang, P. Cheng, X.-C. Ma, X.-L. Zou, W.-H. Duan, J.-F. Jia, and Q.-K. Xue, Phys. Rev. Lett. **101**, 197208 (2008).
[15] L. Gao, W. Ji, Y. B. Hu, Z. H. Cheng, Z. T. Deng, Q. Liu, N. Jiang, X. Lin, W. Guo, S. X. Du, W. A. Hofer, X. C. Xie, and H.-J. Gao, Phys. Rev. Lett. **99**, 106402 (2007).
[16] Y.-S. Fu, S.-H. Ji, X. Chen, X.-C. Ma, R. Wu, C.-C. Wang, W.-H. Duan, X.-H. Qiu, B. Sun, P. Zhang, J.-F. Jia, and Q.-K. Xue, Phys. Rev. Lett. **99**, 256601 (2007).
[17] A. Zhao, Q. Li, L. Chen, H. Xiang, W. Wang, S. Pan, B. Wang, X. Xiao, J. Yang, J. G. Hou, and Q. Zhu, Science **309**, 1542 (2005).
[18] J. van den Brink and A. F. Morpurgo, Nature (London) **450**, 177 (2007).
[19] S. Heutz, C. Mitra, W. Wu, A. Fisher, A. Kerridge, M. Stoneham, A. H. Harker, J. Gardener, H.-H. Tseng, T. Jones, C. Renner, and G. Aeppli, Adv. Mater. **19**, 3618 (2007).
[20] M. Cinchetti, K. Heimer, J.-P. Wustenberg, O. Andreyev, M. Bauer, S. Lach, C. Ziegler, Y. Gao, and M. Aeschlimann, Nature

Mater. **8**, 115 (2009).
[21] P. Gambardella, S. S. Dhesi, S. Gardonio, C. Grazioli, P. Ohresser, and C. Carbone, Phys. Rev. Lett. **88**, 047202 (2002).
[22] H. Brune and P. Gambardella, Surf. Sci. **603**, 1812 (2009).
[23] R. Wu and A. J. Freeman, Phys. Rev. Lett. **73**, 1994 (1994).
[24] J. Stöhr and H. König, Phys. Rev. Lett. **75**, 3748 (1995).
[25] O. Šipr, J. Minár, and H. Ebert, EPL **87**, 67007 (2009).
[26] P. Sainctavit, M.-A. Arrio, and C. Brouder, Phys. Rev. B **52**, 12766 (1995).
[27] J. van Elp and B. G. Searle, J. Electron Spectrosc. Relat. Phenom. **86**, 93 (1997).
[28] J. P. Crocombette, B. T. Thole, and F. Jollet, J. Phys.: Condens. Matter **8**, 4095 (1996).
[29] A. Mugarza, N. Lorente, P. Ordejon, C. Krull, S. Stepanow, M.-L. Bocquet, J. Fraxedas, G. Ceballos, and P. Gambardella (unpublished).
[30] P. Gambardella, S. Rusponi, M. Veronese, S. Dhesi, C. Grazioli, A. Dallmeyer, I. Cabria, R. Zeller, P. Dederichs, K. Kern, C. Carbone, and H. Brune, Science **300**, 1130 (2003).
[31] R. D. Cowan, *The Theory of Atomic Structure and Spectra* (University of California Press, Berkeley, 1981).
[32] F. de Groot and A. Kotani, *Core Level Spectroscopy of Solids* (CRC Press, Cleveland, 2008).
[33] G. van der Laan and B. T. Thole, Phys. Rev. B **43**, 13401 (1991).
[34] R. Prabakaran, R. Kesavamoorthy, G. L. N. Reddy, and F. P. Xavier, Phys. Status Solidi B **229**, 1175 (2002).
[35] E. Koch, Y. Jugnet, and F. Himpsel, Chem. Phys. Lett. **116**, 7 (1985).
[36] G. Dufour, C. Poncey, F. Rochet, H. Roulet, S. Iacobucci, M. Sacchi, F. Yubero, N. Motta, M. N. Piancastelli, A. Sgarlata, and M. D. Crescenzi, J. Electron Spectrosc. Relat. Phenom. **76**, 219 (1995).
[37] S. Carniato, Y. Luo, and H. Ågren, Phys. Rev. B **63**, 085105 (2001).
[38] B. Thole, G. van der Laan, and P. Butler, Chem. Phys. Lett. **149**, 295 (1988).
[39] P. S. Miedema, S. Stepanow, P. Gambardella, and F. M. F. de Groot, J. Phys.: Conf. Ser. **190**, 012143 (2009).
[40] M. D. Kuz'min, R. Hayn, and V. Oison, Phys. Rev. B **79**, 024413 (2009).
[41] T. Kroll, V. Y. Aristov, O. V. Molodtsova, Y. A. Ossipyan, D. V. Vyalikh, B. Büchner, and M. Knupfer, J. Phys. Chem. A **113**, 8917 (2009).
[42] A. Ruocco, F. Evangelista, R. Gotter, A. Attili, and G. Stefani, J. Phys. Chem. C **112**, 2016 (2008).
[43] S. E. Harrison and J. M. Assour, J. Chem. Phys. **40**, 365 (1964).
[44] A. Rosa and E. J. Baerends, Inorg. Chem. **33**, 584 (1994).
[45] B. T. Thole, P. Carra, F. Sette, and G. van der Laan, Phys. Rev. Lett. **68**, 1943 (1992).
[46] P. Carra, B. T. Thole, M. Altarelli, and X. Wang, Phys. Rev. Lett. **70**, 694 (1993).
[47] C. T. Chen, Y. U. Idzerda, H.-J. Lin, N. V. Smith, G. Meigs, E. Chaban, G. H. Ho, E. Pellegrin, and F. Sette, Phys. Rev. Lett. **75**, 152 (1995).
[48] J. Stöhr and D. A. Outka, Phys. Rev. B **36**, 7891 (1987).
[49] C. Brouder, J. Phys.: Condens. Matter **2**, 701 (1990).
[50] G. van der Laan, Phys. Rev. B **57**, 5250 (1998).
[51] I. B. Bersuker, *Electronic Structure and Properties of Transition Metal Compounds: Introduction to the Theory* (Wiley, New York, 1996).
[52] B. T. Thole and G. van der Laan, Phys. Rev. B **38**, 3158 (1988).
[53] G. van der Laan and B. T. Thole, Phys. Rev. Lett. **60**, 1977 (1988).
[54] G. van der Laan and B. T. Thole, J. Electron Spectrosc. Relat. Phenom. **86**, 57 (1997).